

# Sweep Angle Effects of Flow Over an Undulated Cylinder

Trevor K. Dunt\*

*University of Wisconsin–Madison, Madison, WI, 53706*

Christin T. Murphy†

*Naval Undersea Warfare Center–Newport, Newport, RI, 02841*

Ondřej Ferčák‡ and Raúl Bayoán Cal§

*Portland State University, Portland, OR, 97201*

Jennifer A. Franck¶

*University of Wisconsin–Madison, Madison, WI, 53706*

Flow over a seal whisker-inspired undulated cylinder at swept back angles is computationally investigated, comparing the vortex shedding, forces, and wake characteristics to those of an equivalent smooth geometry. Numerous prior studies have demonstrated that undulated cylinders can reduce mean drag and unsteady lift oscillations; however, none have isolated the effects of sweep resulting from whisker positioning in flow. Relevant not only to understanding seal whiskers, such findings are also useful in engineering structural applications to reduce drag and vortex-induced vibration. This investigation performs direct numerical simulation of flow across a rigid, infinite-span, undulated cylinder at sweep angles from 0 to 60° and at Reynolds numbers of 250 and 500. At zero sweep, the undulated cylinder breaks up coherent two-dimensional vortices, having the effect of reducing drag by 10.4% and root mean square lift by 91.2% compared to a smooth elliptical cylinder. With sweep added, the prominence of spanwise vortex breakup and force suppression is reduced, approximating flow over smooth ellipse geometry as sweep increases. At low sweep angles of 15 and 30 degrees, lift is still suppressed by 75.5% and 50% while drag results in a smaller difference of 7.4 and 1.9% reduction from a smooth ellipse.

## I. Introduction

The flow physics and force reduction properties of swept flow over a seal whisker-inspired undulated cylinder geometry are explored. Distinct from the smooth whiskers of other mammals, most species of seal have undulated whiskers that consist of two sets of opposing undulations pictured in Figure 1. The undulated whisker shape enhances a

---

\*PhD Candidate, Nuclear Engineering & Engineering Physics

†Head, Bioinspired Research and Development Lab

‡PhD Candidate, Mechanical & Materials Engineering

§Professor, Mechanical & Materials Engineering

¶Associate Professor, Mechanical Engineering

seals' excellent navigation and prey tracking abilities enabled through hydrodynamic sensing [1–3]. This capability comes from the observation that seal whiskers significantly reduce drag and oscillating lift forces compared to smooth whiskers, improving their effective signal to noise ratio when sensing their environment [4, 5]. Despite a rich background in research [6, 7] that includes whisker anatomy and sensing abilities [1–3], as well as investigations into how whisker shape produces unique flow effects [3–5, 8–24], the influence of sweep angle, defined as the angle with which whiskers are swept back relative to the freestream flow relative to their perpendicular orientation before sweep, is yet to be investigated. An important overlapping field of study is the flow at swept (or yaw) angles over bluff-bodies, which is of interest in multiple disciplines from aerodynamics to civil engineering [25–33].

A common feature in research of seal whisker-inspired geometry is the variation in—and impact of—geometric parameters of the surface. A description commonly used in fluid dynamics investigations is the whisker model introduced by Hanke et al. [4] which was based on measurements of excised harbor seal whiskers. Defined by two angled ellipse cross sections, a seven variable parametric description of the three-dimensional surface was created. From this, Lyons et al. [5] redefined the model into independent variables and established a variable ranking based on hydrodynamic relevance [5]. The geometric variables that produced the most significant impact on forces, shown in Figure 1, were wavelength, aspect ratio, and undulation amplitudes. Other studies performed analysis focusing on specific geometric parameters such as undulation wavelength to probe its impact on vortex shedding, forces, and shedding frequency [13, 24, 34, 35]. These studies established the capabilities of the whisker-inspired geometry which may be extended to applications beyond those found in the original biological system.

Whiskers in the field experience a wide range of flow directions, speeds, and non-uniformity in their tumultuous flow environment. Angle of attack effects (rotation about the  $z$ -axis) have been investigated previously for span-perpendicular flow, finding that reduced forces are most prevalent at zero angle of attack while the flow response increasingly approximates flow over a bluff body as the angle of attack reaches 90 degrees [10, 20, 36]. Whiskers also encounter variation in incoming flow angle due in equal parts to their natural curvature, bending in response to incoming flow, and due to a seals' ability to influence their orientation via their facial musculature. Thus, this research explores the hydrodynamics properties of flow at oblique angles to the whisker span, defined commonly as swept angle in aerodynamics or yaw angle in bluff bodies.

Sweep angle, defined by  $\Lambda$  in Figure 1, where  $\Lambda = 0$  corresponds to the perpendicular flow investigated in prior research, is comparable to research of bluff body flow behavior with a spanwise velocity component. Previous exploration of swept flow drew comparisons to the ubiquitous problem of crossflow over a circular cylinder and include experiments [25–29], often dependent on finite aspect ratio and end effects, and simulations [29–33] over a range of Reynolds number regimes. These studies often test the "crossflow principle" or "independence principle" [37] which estimates the effects of sweep on fluid forces and shedding characteristics by scaling perpendicular flow values proportionally to the normal component of flow over a swept body. This idea does not take into account three-dimensional flow effects, but can still

give reasonable estimates of forces for rigid cylinders with minimal end condition effects, and for a range of sweep angles generally limited to less than or equal to 45 degrees [25, 26, 28, 30–32].

Through simulation of flow over an infinite-span whisker model within a range of sweep angles from 0 to 60 degrees, this paper investigates how sweep impacts the force-reduction properties of an undulated cylinder. The following sections are organized into Section II where the whisker geometry, numerical model, and flow parameters are introduced, Section III in which results are summarized, and Section IV which contains concluding remarks.

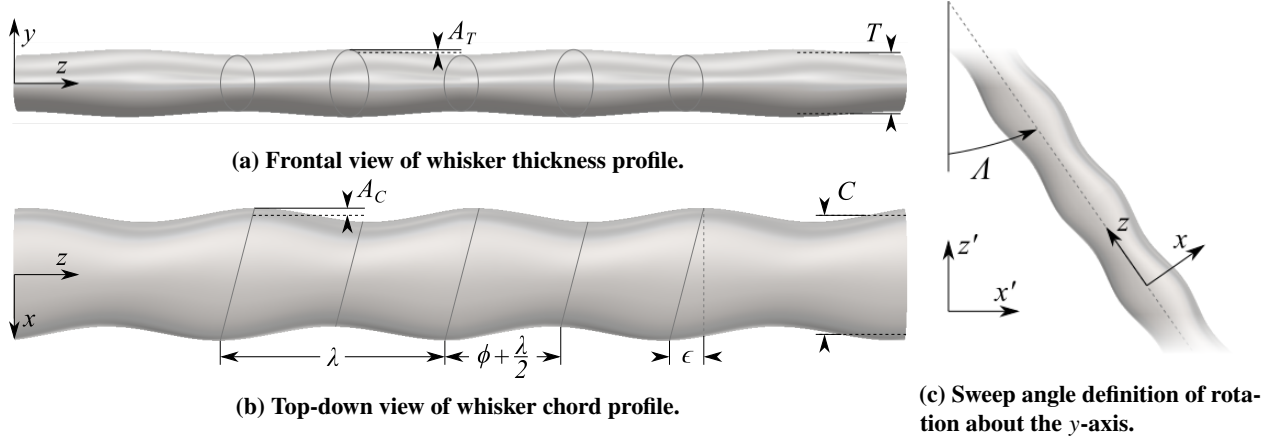


**Fig. 1** Geometric variables comprising the undulated cylinder model as defined by Lyons et al. [5].

## II. Methods

This research computes the time-dependent and three-dimensional flow around an undulated cylinder at various inflow sweep angles. The governing equations are the non-dimensional and incompressible Navier-Stokes equations,

$$\frac{\partial \mathbf{u}}{\partial t} + \mathbf{u} \cdot \nabla \mathbf{u} = -\nabla p + \frac{1}{Re} \nabla^2 \mathbf{u} \quad (1)$$

and

$$\nabla \cdot \mathbf{u} = 0, \quad (2)$$

where  $\mathbf{u}$  is the normalized velocity vector, and  $p$  and  $t$  are non-dimensional pressure and time. Quantities are normalized by the characteristic freestream velocity  $U_\infty$  and the mean thickness of the cylinder,  $T$ . The Reynolds number is thus defined as

$$Re = \frac{U_\infty T}{\nu}, \quad (3)$$

where  $\nu$  is the kinematic viscosity of the fluid.

The numerical solution is discretized using *OpenFOAM* [38] second-order finite volume libraries, and solved with a pressure-implicit split-operator (PISO) algorithm. The numerical method follows that of prior work [13, 34, 35].

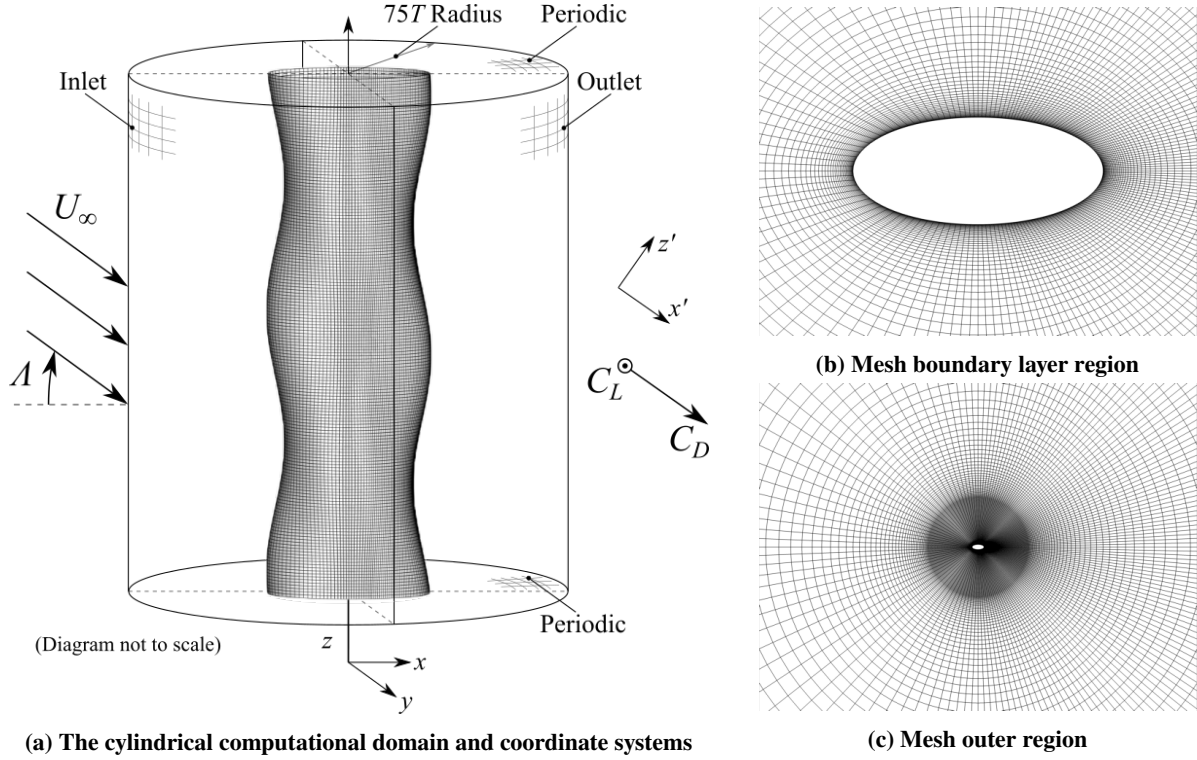


**Fig. 2 Undulated cylinder computational domain and radial mesh cell distribution.**

The undulated geometry is comprised of two sets of undulations, one in the chord ( $x$ -direction), and another in the thickness ( $y$ -direction), as seen in Figure 1. The surface undulations are prescribed from the hydrodynamically relevant non-dimensional parameters developed by Lyons et al. [5] with mean thickness  $T = 1$ , aspect ratio  $\gamma = C/T = 1.919$ , wavelength  $\lambda/T = 3.434$ , transverse amplitude  $A_T/T = 0.09$ , streamwise amplitude  $A_C/T = 0.23$ , undulation offset  $\epsilon = 0.34$ , and undulation symmetry  $\phi = 0.015$ . These values yield a surface with the same measurements as that originally defined by Hanke et al. [4], and the conversion between the two geometric definitions is provided in Lyons et al.

The analytical surface of the whisker is generated and defined using the mesh morphing algorithm described by Yuasa et al. [13]. Starting from a circular cylinder computational domain with a radially structured mesh, the algorithm radially translates the surface mesh nodes to morph the cylinder into a whisker geometry with the specified geometric features defined above. The result is a body-fitted, structured mesh of an undulated cylinder that is repeatable and independent of changes to the starting cylinder mesh resolution.

The computational domain, shown in Figure 2a, consists of an outer cylinder with a radius of  $75T$ . The outer boundary is divided into an upstream inlet with uniform velocity and zero-gradient pressure and a downstream,



zero-gradient velocity and fixed pressure outlet. The model span consists of two wavelengths of the undulated cylinder, with periodic boundary conditions in the  $z$ -direction.

The domain is held constant through a range of swept angle flows which are created by an angled inlet velocity at angle  $\Lambda$  with  $\Lambda = 0$  corresponding to flow normal to the cylinder span. Due to the phase difference in leading and trailing edge undulations, the geometry possesses a directional bias relative to the sign of sweep angle. The positive  $\Lambda$  direction is chosen such that angled flow is in line with the angled ellipses that define the whisker surface as visible in Figure 1. In the current investigation, only the positive (aligned with the undulation offset  $\epsilon$ ) range of sweep angle  $\Lambda$  is explored.

The cylindrical structured mesh shown in Figure 2a consists of 170 cells in the spanwise direction resulting in a spanwise resolution of  $\Delta z/T = 0.041$ , 160 about the azimuthal direction, and 154 in the radial direction which are initially clustered to produce a minimum cell thickness of  $\Delta r/T = 0.003$  and radial resolution of  $\Delta\theta = 4.01^\circ$ . While the mesh and computational domain have been previously validated at zero sweep angle [13, 34], a mesh independence study at sweep angle  $\Lambda = 60$  is documented in Section A.

Simulations are performed at Reynolds numbers of 250 and 500, which are biologically relevant based on seal swimming speeds and average whisker diameter [39]. Simulation time is specified in non-dimensional convective time units (CTU), or the time it takes for the flow to move one mean thickness at freestream velocity. All simulations begin with an initial transient time of 100 CTU to allow ample time for the flow to fully develop. After this point, a subsequent 400 CTU are simulated and utilized for all averaged quantities.

Forces due to pressure and skin friction are computed along the whisker surface as a function of time, and are used to compute the lift and drag coefficients. As sweep angle rotation occurs in the  $xz$  plane, the magnitude of lift forces oscillating parallel to the  $y$ -axis require no rotation, whereas drag force will shift directions with changes in  $\Lambda$  and is thus defined parallel to the freestream flow. The drag and lift coefficients are given by

$$C_D = \frac{2F_D}{\rho U_\infty^2 T L_z} \quad C_L = \frac{2F_L}{\rho U_\infty^2 C L_z} \quad (4)$$

where drag force is normalized by the whisker mean thickness  $T$  (frontal area in the  $yz$  plane), and lift is normalized by the mean chord length  $C$  (an average area in  $xz$ ). As these forces constantly oscillate in response to vortex shedding, force comparison between orientations is facilitated by mean values of drag. As the whisker geometry lacks camber and is symmetric about the  $xz$  plane, lift forces oscillate about zero. The magnitude of oscillations is captured by the root mean square (RMS) of the coefficient over  $n$  samples in time with a sampling rate of 50 samples per convective time unit,

$$C_{L,RMS} = \sqrt{\frac{1}{n} \sum_{i=1}^n C_{L_i}^2} \quad (5)$$

To provide a baseline comparison for forces measured from whisker-inspired undulated cylinder geometry, simulations

of flow over a circular cylinder and elliptical cylinder are also performed. The circular cylinder maintains the same mean thickness (diameter) as the undulated geometry while the ellipse has the same mean aspect ratio. The elliptical cylinder captures the effect of a streamlined cross-section and serves as a useful intermediate comparison between a circular cylinder and the undulated cylinder.

For flow visualization,  $Q$ -criterion is calculated to identify vortices in the wake by relating the magnitude of local strain rate  $\mathbf{S} = \frac{1}{2}(\nabla\mathbf{u} + \nabla\mathbf{u}^T)$  and rotation rate  $\mathbf{\Omega} = \frac{1}{2}(\nabla\mathbf{u} - \nabla\mathbf{u}^T)$  tensors in the equation,

$$Q = \frac{1}{2}(\|\mathbf{\Omega}\|^2 - \|\mathbf{S}\|^2). \quad (6)$$

Lastly, the distribution of energy in the wake is compared via contours of turbulent kinetic energy (TKE), defined by the half-sum of variances  $\overline{(\mathbf{u}')^2}$  in fluctuating velocity  $\mathbf{u}'$  obtained by subtracting time averaged velocity  $\bar{\mathbf{u}}$  from instantaneous velocity  $\mathbf{u}(t)$ .

$$k = \frac{1}{2} \left[ \overline{(u')^2} + \overline{(v')^2} + \overline{(w')^2} \right] \quad (7)$$

### III. Results

#### A. Effect of Sweep Angle on Fluid Forces

The time averaged coefficient of drag and root mean square lift coefficient are reported in Figure 3 for the three geometries and five sweep angle values at  $Re = 250$ . Focusing first on the two smooth geometries of the cylinder and ellipse, there is a clear decrease in forces with respect to increasing sweep angle. The cylinder's initial drag coefficient of 1.31 decreases to 0.33 when swept at 60 degrees, whereas the streamlined ellipse has  $C_D = 0.89$  for perpendicular flow and  $C_D = 0.26$  at  $\Lambda = 60$  degrees. Both smooth geometries closely follow a descending cosine curve as theorized by the independence principle [37], plotted as dashed curves in Figure 3a. The model works well for smooth geometries since the decrease in the perpendicular flow component is responsible for separation and regular vortex shedding, the prominent source of drag force.

At  $\Lambda = 0$ , the whisker geometry exhibits strong drag reduction with respect to a cylinder (37.9%) and a smaller reduction compared to an ellipse (8.6%). However, as sweep angle increases, the magnitude of drag forces for the whisker geometry quickly merges with and becomes indistinct from the smooth ellipse at  $\Lambda = 30$  and beyond, with both aligning with the circular cylinder at  $\Lambda = 60$ . Thus, drag coefficient due to the undulated surface is only reduced when ( $\Lambda < 30$ ).

Observing unsteady lift amplitude in Figure 3b, a circular cylinder and ellipse exhibit a large difference at  $\Lambda = 0$  with RMS coefficients of 0.27 and 0.11, respectively. As sweep is added, this difference narrows as their forces both decline. Contrasting with drag force, the prediction of lift forces is less accurately approximated by the independence

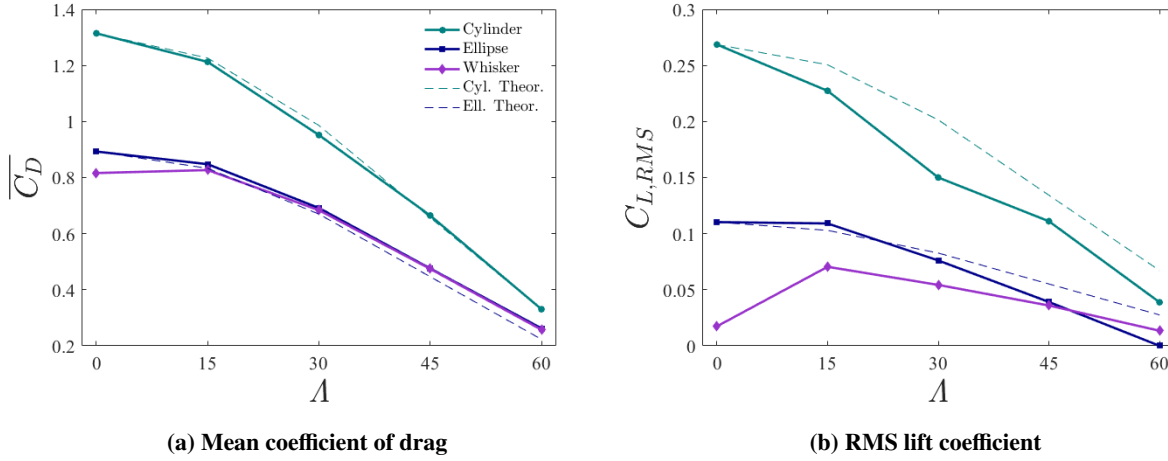


**Fig. 3** Time-averaged drag and root mean square lift coefficient values for the circular cylinder, ellipse, and undulated whisker geometry with respect to sweep angle at  $Re = 250$ . Included as dashed curves are predictions of the forces based on the perpendicular value scaled by cosine of velocity as theorized by the independence principle [37].

principle. This is likely due to a greater dependence on swept vortex shedding characteristics and spanwise effects flow effects that do not develop commensurately to the normal velocity component.

Unlike drag, the root mean square lift exhibits stark differences between the whisker and ellipse. For perpendicular flow, the undulated surface drastically reduces  $C_{L,RMS}$  compared to a circular cylinder and ellipse alike, with a reduction of 93.5 and 84.2%. Unlike the behavior of the smooth geometries, the whisker  $C_{L,RMS}$  increases with low sweep angles, rising from 0.02 at  $\Lambda = 0$  to 0.07 at  $\Lambda = 15$ . This still maintains a significantly smaller amplitude than an ellipse with a reduction of 35.4%. The  $C_{L,RMS}$  value remains below an ellipse until a sweep angle of  $\Lambda = 45$  at which point values for an ellipse and whisker are roughly equivalent. This suggests that a point of diminishing returns in the effectiveness of the modeled whisker-inspired undulations exists at or near this sweep angle. At  $\Lambda = 60$ , the undulated surface  $C_{L,RMS}$  is higher than the ellipse though still below the circular cylinder and ellipse model.

Simulations are also performed at a higher Reynolds number of 500 where similar results in forces are observed in Figure 4. In agreement with  $Re = 250$ , drag coefficient decreases with increasing sweep angle for all geometries. The circular cylinder and ellipse once again demonstrate disparate drag coefficients in perpendicular flow of  $C_D = 1.17$  and 0.80 and almost converged coefficients of 0.25 and 0.22 at  $\Lambda = 60$ . Both sets of coefficients still follow the predicted decreasing curve of the independence principle, however the prediction of drag force is most accurate while lift force has a greater deviation particularly at the largest sweep angles.

At  $Re = 500$ , the whisker geometry experiences an increase in the effective drag reduction from an ellipse. In perpendicular flow, in drag coefficient coefficient is reduced by 10.4% compared to a previous 8.6%. The drag suppression also persists to a greater extent at 7.4% for  $\Lambda = 15$  where, previously in Figure 3, drag forces were observed to more quickly merge with ellipse force values at this angle. At  $\Lambda = 30$ , a similar effect as the  $Re = 250$  simulations

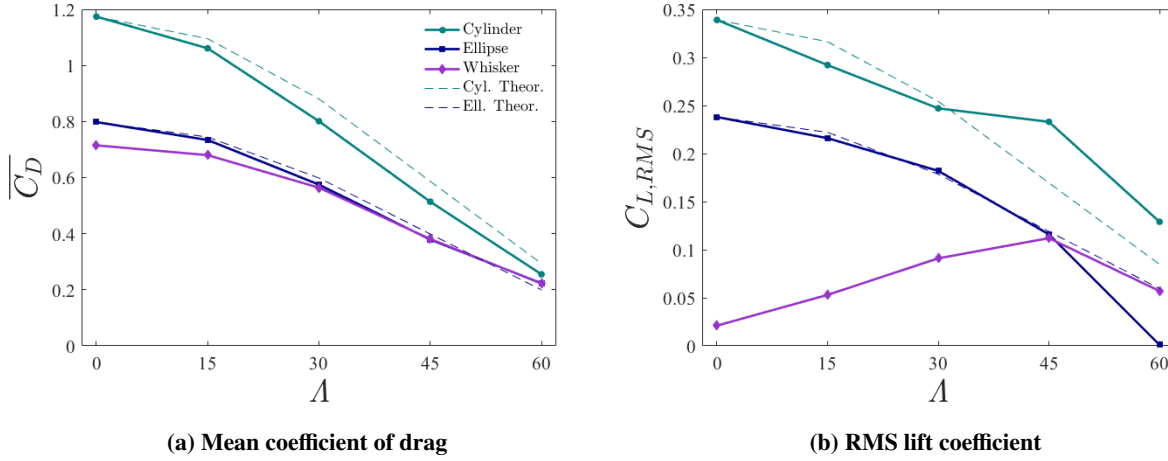
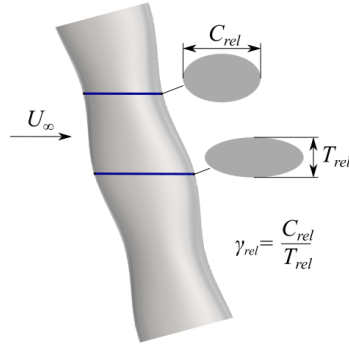


**Fig. 4** Averaged force coefficient values for the cylinder, ellipse, and whisker geometries with respect to sweep angle at  $Re = 500$  as well as theoretical values of cylinder and ellipse forces based on the independence principle.

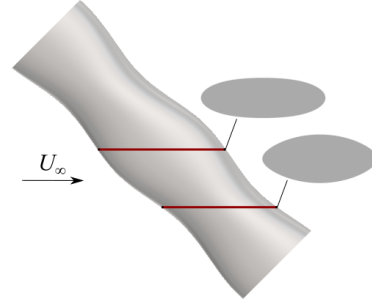
returns as the whisker geometry reaches a similar drag coefficient as the ellipse up to  $\Lambda = 60$ .

Lift forces at  $Re = 500$  on the smooth cylinder and ellipse both experience a general increase over their  $Re = 250$  counterpart. Values of  $C_{L,RMS} = 0.34$  for a cylinder and 0.24 for an ellipse at  $\Lambda = 0$  both decrease with added sweep. The most interesting observation is the stronger  $C_{L,RMS}$  suppression of the undulated cylinder at  $Re = 500$ . For the perpendicular flow orientation, the whisker's lift RMS coefficient of 0.021 is a 91.2% decrease from an ellipse. Again, conversely to the smooth comparison geometries, the whisker geometry shows an increasing  $C_{L,RMS}$  with the addition of sweep at low angles. Despite this, at  $\Lambda = 15$  the undulated surface is responsible for a 75.5% reduction in lift force from the ellipse, and 50.0% at  $\Lambda = 30$ . Similarly to the  $Re = 250$  simulations, the ellipse and whisker converge at  $\Lambda = 45$  and again diverge at  $\Lambda = 60$ .

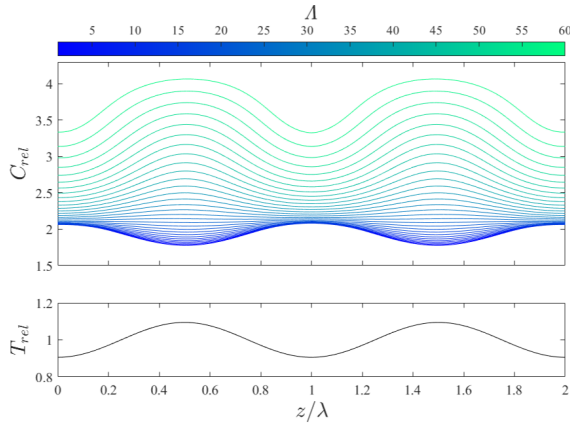
To understand the force observations of the undulated cylinder, Figure 5 describes the interaction between sweep angle and the relative cross section. While possessing the same mean chord length, thickness, and resulting mean aspect ratio as the smooth ellipse geometry, the piece-wise sinusoidal surfaces of the whisker geometry vary the effective value of these parameters with respect to spanwise location and orientation. Figure 5c displays the relative thickness,  $T_{rel}$  and chord length  $C_{rel}$  as a function of span,  $z$ . As shown in the  $T_{rel}$  plot, thickness varies with location along the whisker surface, however its magnitude is unaffected by sweep angle. Conversely, relative chord length is dependent on orientation and location. As with a smooth geometry, the overall magnitude of chord length increases with sweep, though the shape of its periodic variation changes. With no sweep angle, the location of maximum chord length aligns with the minimum thickness and vice versa. This relationship gradually changes as sweep angle increases, where at approximately 30 degrees the chord length profile flattens and then reverses its original trend afterwards where maximum chord length and thickness now coincide. These trends are a result of the  $180^\circ$  phase difference between thickness and chord undulations as well as the smaller phase difference between leading and trailing undulations in chord length.



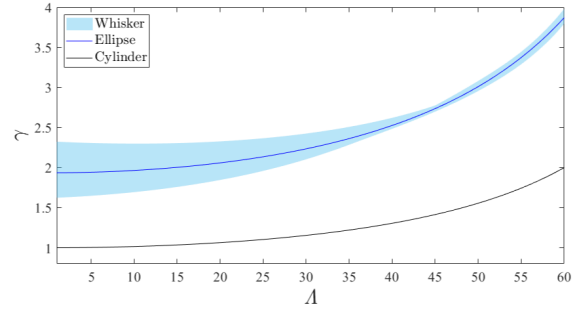
(a) Relative chord and thickness at  $\Lambda = 15$



(b) Relative chord and thickness at  $\Lambda = 45$



(c) Variation in chord length  $C$  and thickness  $T$



(d) Aspect ratio as a function of sweep: Whisker min/max variation across spanwise positions

**Fig. 5 Sweep-dependent spanwise variation in geometry cross section parallel to incoming flow.**

Together, these two dimensions create hydrodynamically important effects on the relative aspect ratio of the undulated cylinder, and can explain trends in the forces. In Figure 5d, the sweep angle-dependent aspect ratio of the whisker geometry is represented as a vertical range. It is widest at zero sweep angle as the undulation phase difference along the  $z$ -axis creates cross-sections of thicker, round cylinder-like geometry alternating with regions that have a longer streamlined cross-section. As sweep angle increases, the undulation phase difference relative to sweep is reduced and then reversed, creating an increasingly uniform cross-section across the span. The range of deviation from the mean reaches a minimum at approximately 45 degrees, converging with the ellipse geometry and notably approximating its flow response and resulting forces which converge between the two geometries at this point.

## **B. Time Averaged Velocity**

Time-averaged velocity profiles near the whisker surface can provide insight into the three-dimensional features of the flow. Imposing a sweep angle introduces a spanwise freestream velocity component which alters flow characteristics of the undulated geometry in distinct ways from the smooth comparison geometries. Visible in Figure 6a, a smooth ellipse demonstrates a separation point that is constant with respect to span and moves downstream moderately with increasing sweep angle.

For the whisker geometry in Figure 6b, streamlines of time-averaged velocity demonstrate the increasing spanwise flow with sweep angle as well as its effect on separation and recirculation near the trailing edge. For the perpendicular flow orientation, streamlines are redirected around areas of increased thickness and converge in regions of increased chord length. Trailing edge streamlines showing reverse flow also highlight a unique separation line that is localized to each wavelength of the whisker surface and creates distinct shedding regions divided in the vicinity of the streamwise undulation peak.

Upon the addition of swept flow, the spanwise flow initiated by geometry undulations is diluted but not eliminated. At 15 degrees, spanwise flow across the surface follows the freestream angle with minor redirection when traversing the streamwise and transverse undulations. Here, the separation line that delineated two distinct wake regions has disappeared and is replaced by a continuous separation region. Although now connected across the entire span, the influence of surface undulations is clear as separation occurs noticeably closer to the trailing edge in the regions of greatest chord length and minimal thickness relative to incoming flow. Recirculating flow near the trailing edge is now more biased in the swept freestream direction, however it still fully reverses in the streamwise direction in regions adjacent to the previously mentioned delayed separation.

This feature is gradually lost as sweep angle increases. For the swept 30, 45, and 60 degree configurations, the separation point moves slightly towards the trailing edge, however, its spanwise variation weakens and settles to a function of the spanwise relative chord length. Additionally, flow behind the separation line gradually transitions from fully reversed in the streamwise direction to roughly perpendicular and later becomes mostly spanwise, increasingly

approximating the spanwise symmetric behavior of smooth geometry. As time-averaged flow becomes increasingly ellipse-like, the change in observed lift and drag coefficient values converges with the ellipse as well.

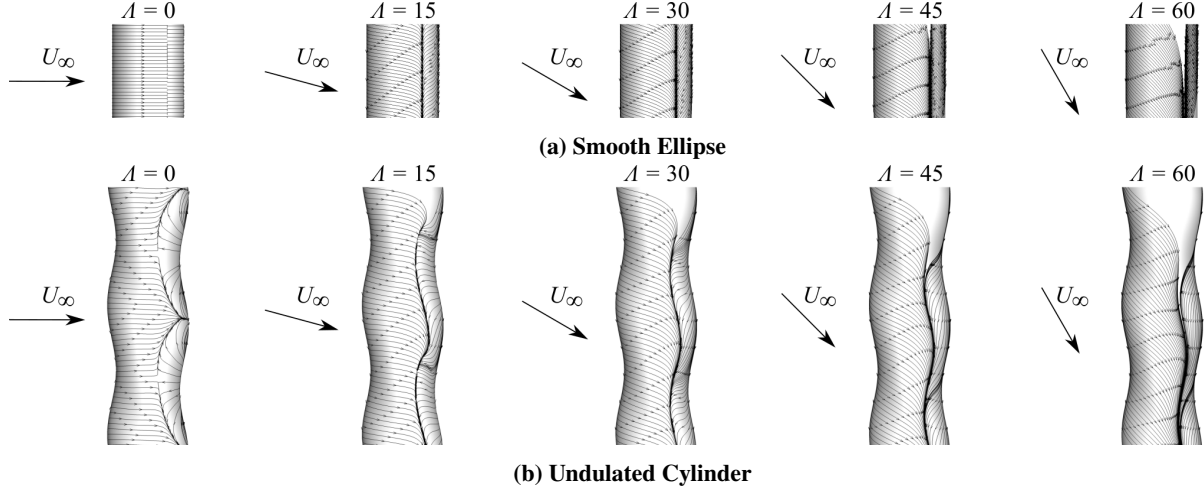


**Fig. 6 Surface streamlines of time averaged velocity  $\bar{u}$ .**

### C. Vortex Wake Effects

Having observed the impact of swept geometry on forces and basic flow measurements, another important feature of whisker geometry is its modification of shed vortices. The flow structures created by the surface undulations are markedly three-dimensional in comparison to the smooth geometry and this has a strong influence on the mixing and dissipation of energy in the wake. To visualize these wake structures, Figure 7 shows isosurfaces of  $Q$ -criterion for the perpendicular and sweep angle flow orientations of the smooth ellipse and whisker geometry at Reynolds number 250.

As increasing sweep angle increases the spanwise velocity component, fluid rotation strength on the axis parallel to the span ( $\omega_z$ ) diminishes. At  $\Lambda = 0$  where rotation is strongest relative to shearing motion in the wake, a larger  $Q$  value captures wake structures effectively for the whisker and ellipse. However, as sweep increases, the same  $Q$  value washes out the weaker wake structures. Thus the value of  $Q$  is scaled relative to the perpendicular flow configuration.

Looking first into the properties of the smooth ellipse, the salient features up to and including the  $\Lambda = 45$  orientation are the spanwise symmetry in shed vortices, decreasing shedding frequency with increasing sweep angle, and primarily two-dimensional behavior relative to the streamwise direction. At the largest sweep angle of  $\Lambda = 60$ , vortices are shed at a shallower angle to incoming flow in a pattern noted for similar flows in prior literature [31].

These observations contrast with the flow structures shown in the wake of the whisker geometry. The seal whisker wake at  $\Lambda = 0$  consists of two distinct shedding regions that correspond to adjacent wavelengths of the whisker surface. This breakup of vortices along the span is a result of spanwise momentum transport over the undulated surface and leads to a noticeable increase in streamwise vorticity as is visible in the wake [5]. Also of note is the alternating phase pattern with which adjacent wavelengths exhibit shedding. Prior literature demonstrated that the presence of this pattern may be

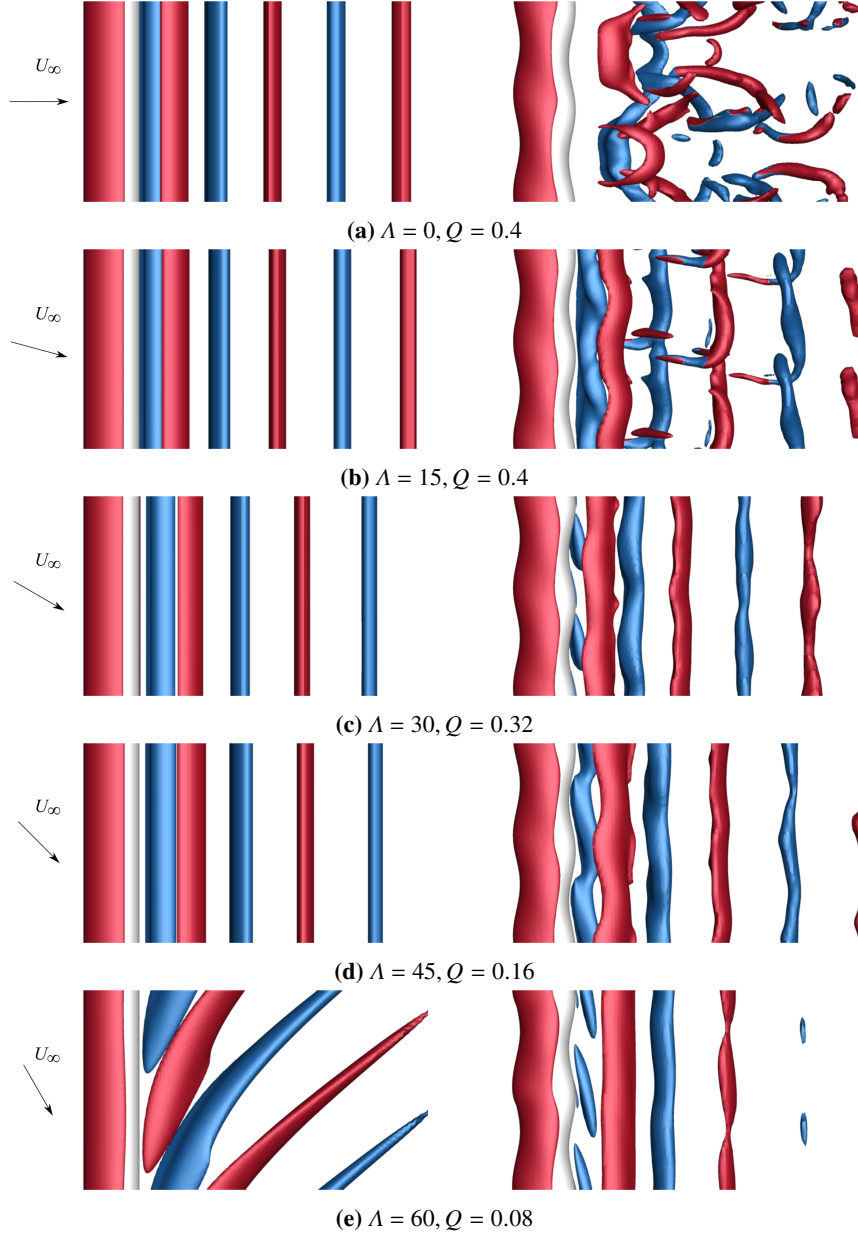
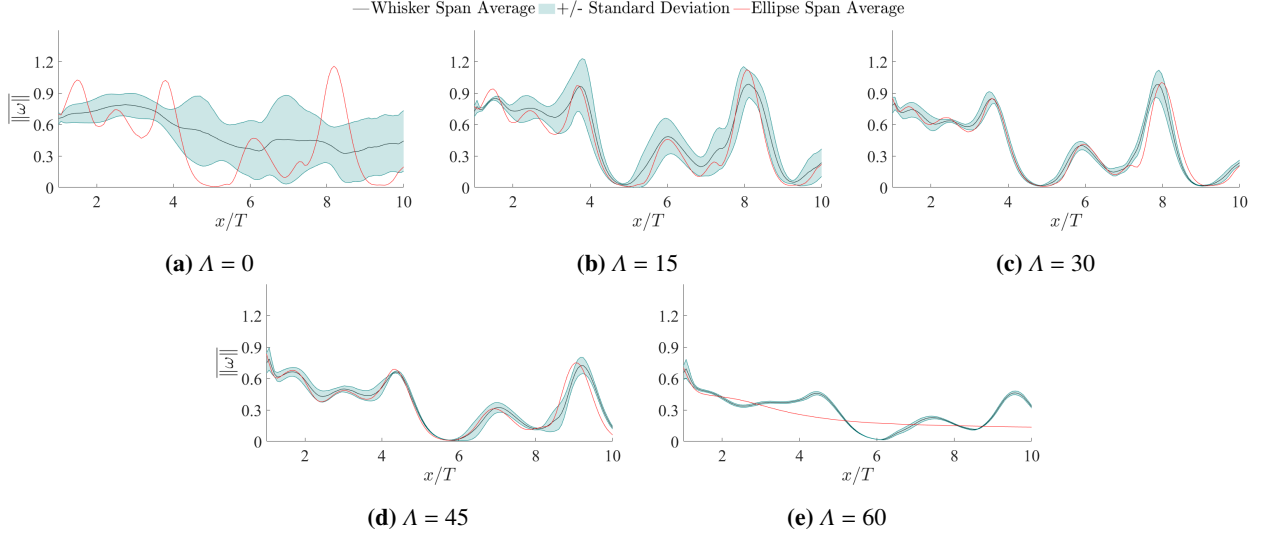


**Fig. 7** Flow structures for  $Re = 250$  visualized by isosurfaces of  $Q$ -criterion colored by the sign of  $Z$ -vorticity.

beneficial to the reduction of fluid forces, but is just one effect in an ensemble of others that produce the resulting lower forces [34, 35]. With the addition of sweep angle, this alternating phase pattern disappears, though some streamwise vorticity with the same spanwise periodicity as the surface undulations is still observable in the wake. In the  $\Lambda = 15$  swept results, due to a directional bias from the added spanwise flow, the streamwise vortex structures are no longer equally sized and their appearance is sensitive to the choice of  $Q$  threshold. Beyond this point at  $\Lambda = 30$  and  $45$ , shed vortices are similar to those created in the wake of the smooth ellipse. There exists some separation between adjacent wavelengths in the near wake that is merged into span-symmetric roller vortices downstream. The ellipse-like behavior



of flow structures also mirrors the converging trends in forces for the middle range of sweep angle values between the two geometries. Finally, for  $\Lambda = 60$ , the whisker geometry is observed to delay the ellipse behavior of peeling off vortex structures at a shallow angle and instead maintains the roller-type structures for a larger sweep. From the perspective of forces, this delayed transition in shedding behavior is less effective at lift suppression compared to the ellipse.



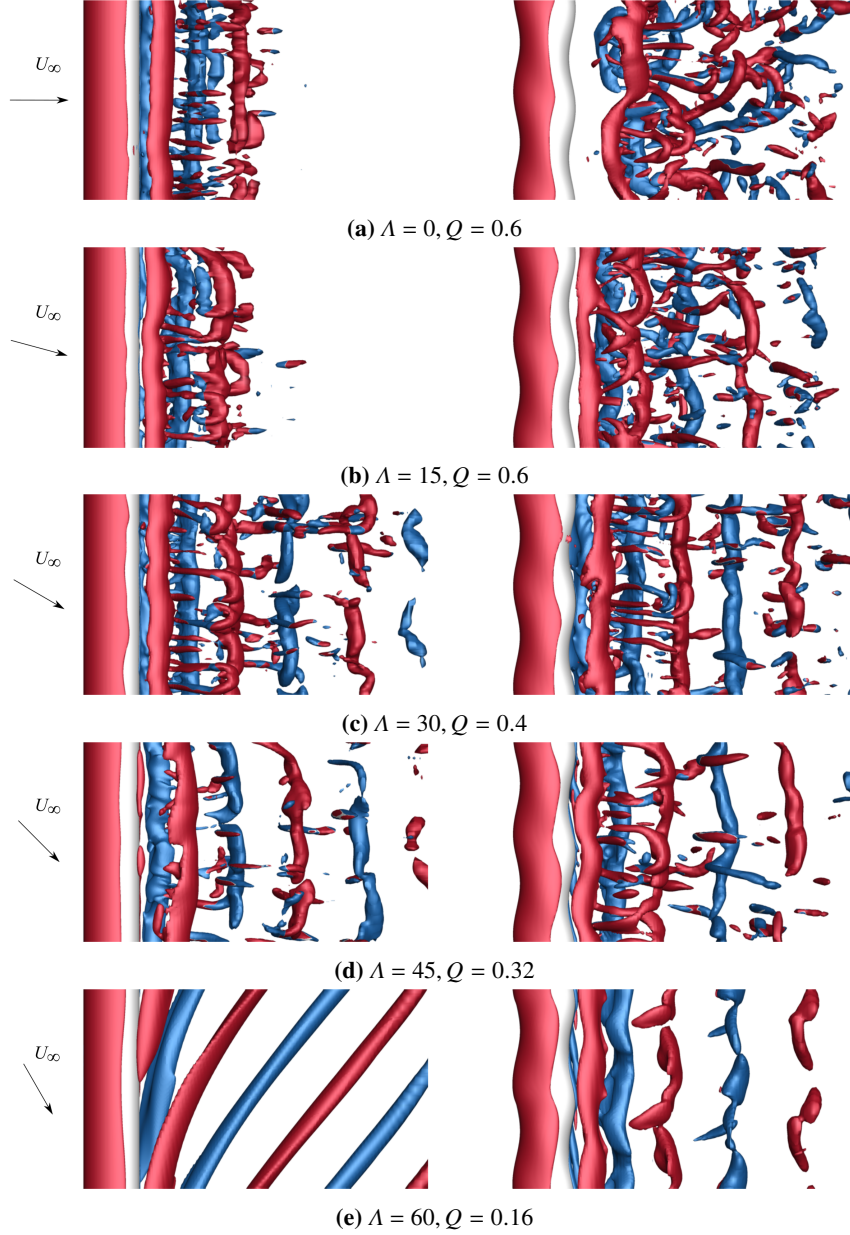
**Fig. 8 Vorticity magnitude averaged over the entire span in  $z$  and a vertical range of  $y/T = 0 - 2$ .**

Figure 8 plots spatially averaged vorticity magnitude in the wake to enable a quantitative comparison of vortex structures. As ellipse geometry did not exhibit spanwise variation in wake structures with the exception of  $\Lambda = 60$ , a single red line on each plot demonstrates the primarily  $z$ -oriented vorticity resulting from roller-type vortices. The whisker geometry, particularly for  $\Lambda = 0$ , instead exhibits strong spanwise variation in shed vortices. Its span average is represented by a black curve and an additional shaded region displays one standard deviation above and below the span-averaged curve highlighting the large spanwise vorticity variation.

Comparing the vorticity magnitude plots to their isosurface counterparts, at  $\Lambda = 0$  roller vortices shed by an ellipse result in a periodic pattern of peaks in vorticity magnitude corresponding to isosurfaces of negative  $\omega_z$ . The vorticity magnitude of the whisker geometry departs significantly from this pattern in both the near and far wake. The disruption of rollers into the spanwise phase-shifted horseshoe vortex pattern results in a lower average vorticity magnitude close to the trailing edge than an ellipse and a misalignment of peaks with those observed for an ellipses' roller vortices.

At  $\Lambda = 15$  the mean vorticity magnitude between the two geometries converges to a similar pattern of periodic peaks with the standard deviation decreasing compared to  $\Lambda = 0$ . While some variation in peak heights remain, the ellipse span-average curve is generally contained within one standard deviation of the whiskers' span-averaged magnitude. The gradual increase in wake similarity continues for  $\Lambda = 30 - 45$  as the increasing spanwise component of velocity causes the whisker geometry to more closely emulate the span-symmetric flow over an ellipse. Finally, at  $\Lambda = 60$  the transition

in shedding patterns experienced by the ellipse results in a constantly decreasing mean vorticity magnitude after the near wake region. In contrast, the whisker geometry continues to demonstrate peaks consistent with its roller-type vortex street shedding pattern, features which will influence the distribution and dissipation of energy in the wake in later analyses and explain the difference in RMS lift coefficient at  $\Lambda = 60$  where the undulated cylinder exceeded the ellipse.



**Fig. 9** Isosurfaces of  $Q$ -criterion colored by the sign of  $Z$ -vorticity for  $Re = 500$ .

To enable a comparison,  $Q$ -criterion at  $Re = 500$  are shown in Figure 9. At this higher Reynolds number, all wakes demonstrate increased vortex strength and, for ease of visualization, are plotted using larger  $Q$  values than the  $Re = 250$  data. The wake also exhibits increased local turbulence demonstrated by the finer and more complex  $Q$

structures. Additionally, spanwise instabilities characteristic of the flow regime are prevalent, particularly visible for the ellipse in the form of many streamwise finger-like structures along the span, and not present at  $Re = 250$ . However, with these developments, the ellipse still maintains a vortex street shedding pattern up until angle  $\Lambda = 60$  where the larger component of spanwise velocity again transitions to a separate shedding regime as seen for  $Re = 250$ .

Next, comparing a smooth ellipse and whisker geometry at this higher Reynolds number reveals additional explanations for the force results. First examining a smooth ellipse, particularly for angles  $\Lambda = 0$  and  $15$ , the smooth geometry produces noticeably shortened visible wakes, forming stronger and more compact vortices close to the trailing edge surface reflecting the significantly increased RMS lift coefficient values observed for  $Re = 500$ . In contrast, the undulated cylinder sheds vortices much further from the model surface and continues to exhibit a notable phase difference in the shedding of horseshoe-type vortex structures from adjacent wavelengths at  $\Lambda = 0$ , while experiencing only a small increase in lift coefficient values during the flow regime change. Beyond this point, larger angle orientations once again exhibit increasing spanwise symmetry similar to observations of the  $Re = 250$  simulations as the whisker geometry RMS lift coefficient continually approaches the ellipse. Finally, in the case of  $\Lambda = 60$ , the whisker geometry again appears to delay the transition of flow to a peeling-off regime, instead maintaining more roller-like structures which are reflected in the larger RMS lift coefficient compared to an ellipse at this orientation.

It is worth noting that other studies, e.g. [40], have extended the use of the  $Q$ -criterion by incorporating both positive and negative  $Q$  values in combination with force partitioning methods to enable a deeper dissection of the interplay between vortex dynamics and force generation. These methods highlight the potential for future work in the area of whisker-inspired geometry, particularly in relation to the forces observed as a result three dimensional wake of this complex geometry.

To further explore the effect of the modified flow patterns created by the whisker geometry, turbulent kinetic energy in the wake can be correlated with observed vortex structures. Figure 10 displays contours of TKE with respect to sweep angle in the  $xz$ -plane for  $Re = 250$ . As observed in prior seal whisker literature [34], at  $\Lambda = 0$  the largest values of TKE occur in periodic spanwise regions that align with the streamwise vortex structures visible in Figure 7 and, compared to a smooth ellipse, exhibit a lower peak magnitude and form further downstream in the wake. At  $\Lambda = 15$ , the influence of altered streamwise vortex structures is still visible in contours of TKE where their interference with adjacent structures creates long pairs of horizontal mixing regions.

Also of note is the significant increase in TKE magnitude for the entire sampled region which correlates with the increase in unsteady lift forces observed with the initial addition of sweep angle, contrasting the drop in forces and TKE seen for smooth geometry. Figure 10, column three, demonstrates this observation through span-averaged TKE as a function of  $x/T$ . In Figure 10a, the curves representing the whisker and ellipse show a large decrease in TKE magnitude for the whisker geometry to levels below even that observed for  $\Lambda = 30$ . TKE magnitude decreases with an addition of sweep angle at  $\Lambda = 15$  for the ellipse but initially jumps for the whisker geometry at the same angle, mirroring the

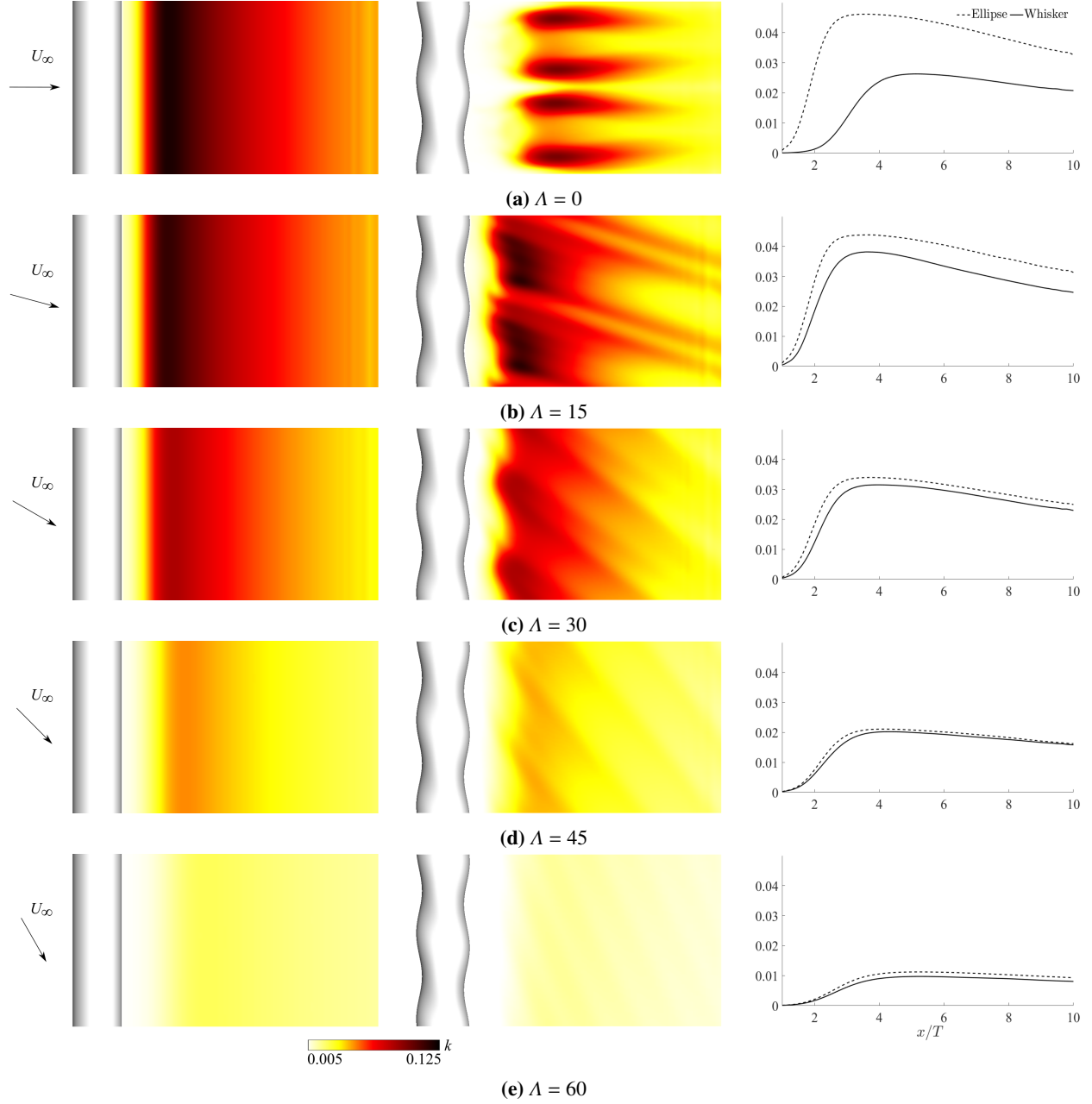


**Fig. 10** Contours of turbulent kinetic energy in the wake accompanied by plots of span-averaged TKE.

behavior of  $Re = 250$  forces discussed previously. Beyond this point, the magnitude of wake TKE decreases steadily with sweep angle to minimum values at  $\Lambda = 60$ .

The  $x$  location at which these peak magnitudes occur is also strongly influenced by geometry prior to sweep and then becomes relatively uniform with increasing angle. Figure 10a demonstrates this increased formation length as the strongest contour levels form much closer to the model surface in the wake of a smooth ellipse. This is also reflected in the TKE magnitude plot where the  $\Lambda = 0$  whisker peak value occurs much further into the wake than the corresponding

ellipse. With added sweep angle, this distance collapses quickly for the whisker as shown by Figure 10b where the highest contours of TKE appear at a similar  $x$  location for both geometries and in the magnitude curves where the peak whisker TKE value occurs at a lower  $x/T$  value that is closer to that of the ellipse peak.

For  $\Lambda = 30$  and beyond, the influence of undulations on increased streamwise vorticity and its disruptive effects on the formation of roller vortices diminishes. A periodic wake TKE pattern is still visible for all large sweep angles, however the magnitude with respect to spanwise location becomes increasingly uniform. For  $\Lambda = 45$ , spanwise momentum transport is now dominated by spanwise flow instead of surface undulations and the resulting wake increasingly mirrors that of an ellipse with roller vortices and the accompanying pattern in TKE as they dissipate. At  $\Lambda = 60$ , as was shown by flow structures in Figure 7, the presence of undulations appears to delay the transition of vortex shedding to a shallow angle regime with a noticeable mismatch from the sweep angle that is also reflected in contours of TKE.

## IV. Conclusion

Numerical simulations of flow over a whisker-inspired geometry are investigated at Reynolds numbers of 250 and 500 over a range of sweep angles. Comparing the whisker geometry to a smooth cylinder results in a significant in unsteady lift and drag forces across the entire range of tested sweep angles. To isolate the effects of the undulated surface, comparison with a smooth ellipse of equivalent dimensions, which also experiences significantly lower forces than a circular cylinder, reveals a reduction of both forces for the range of flow angles of  $\Lambda = 0$  to 45 while  $\Lambda = 60$  showed a slight increase in RMS lift over an ellipse. The impact of surface undulations is strongest in flow perpendicular to the model span with a powerful reduction in RMS lift force by 91.1% and 84.2% from that of a smooth ellipse for the lower and higher Reynolds numbers, respectively. In terms of drag forces, there is a reduction of 10.4% and 8.6%, respectively. As sweep angle increases forces are still reduced, albeit by a smaller magnitude, up to a sweep angle of  $\Lambda = 45$  where the ellipse and whisker converge to similar values before ultimately diverging with a larger whisker lift force at  $\Lambda = 60$ .

The response of the whisker-inspired shape is influenced by the three-dimensional flow driven by its spanwise-varied cross-section demonstrated to have a complex evolution with respect to increasing angle. With larger sweep angle, as the whisker undulations increasingly approximate the relative spanwise symmetry in aspect ratio of an ellipse, the strong spanwise flow effects generated by surface undulations are observed to gradually give way to ellipse-like shedding behavior. This also mirrors the ellipse trend in forces and results in increasingly similar flow structures. While perpendicular flow demonstrated distinct shedding regions along the span visualized by a unique separation line and flow structures with strong streamwise vorticity, large sweep angles merged these shedding regions and approximated the flow structures of a smooth ellipse. The exception is that of the largest sweep angle tested at  $\Lambda = 60$ . Here undulations delayed the transition to a different wake structure. These altered flow patterns were also reflected in contours of turbulent kinetic energy in the wake, which began with concentrated mixing regions that eventually spread and merge across the span similarly to an ellipse.

Based on resulting force measurements, angled whisker-inspired cylinder geometry for sweep angles of  $\Lambda = 30$  or smaller shows the most promise in applications of oscillating lift force and vortex induced vibration reduction and to a lesser extent, the reduction of drag force. Observations made at two bioinspired Reynolds number values indicate that the forces, shedding, and wake structure effects are not strictly sensitive to a specific flow condition within this regime. The extension of this geometry and its beneficial qualities to higher Reynolds numbers is still an open question.

## V. Acknowledgments

The authors acknowledge funding support by the National Science Foundation Award CBET-2035789 (JAF) and CBET-2037582 (RBC), the Naval Research Enterprise Internship Program, and the Department of Defense SMART Scholarship Program. This research was conducted with computational resources at the Department of Defense High Performance Computing Modernization Program and the University of Wisconsin-Madison Center for High Throughput Computing.

DOD Distribution Statement A. Approved for public release: distribution is unlimited.

### A. Mesh Independence

The numerical grid used for these simulations consists of 4.14 million cells and is the same as as the mesh developed and validated in previous literature [5, 13, 34] for simulations at  $Re = 500$  after comparison to structured meshes containing 1, 2, and 6 million cells. Figure A1 shows that,, while still well-resolved, the addition of sweep to the domain produces a larger spanwise component of flow for which the original mesh was not validated.

To ensure that mesh resolution is sufficient to capture physical flow features and align results with those expected from prior literature, a series of mesh resolution levels were simulated at the largest sweep angle of  $\Lambda = 60$  (with its larger spanwise velocity component) to compare their force values and flow field characteristics. The dimensions of the meshes used and resulting values for mean drag coefficient and shedding frequency are given in Table A1. Also shown below in Figure A1 are contours of time-averaged Reynolds stress  $\overline{u'u'}$  at equivalent spanwise locations for each mesh. Given the mesh candidates tested, the variation in forces and flow field features is minimal at and above the 4.14M cell mesh for the worst-case scenario spanwise flow condition. This mesh resolution is therefore chosen once again to minimize computational cost while delivering accurate results for the metrics of interest in this investigation.

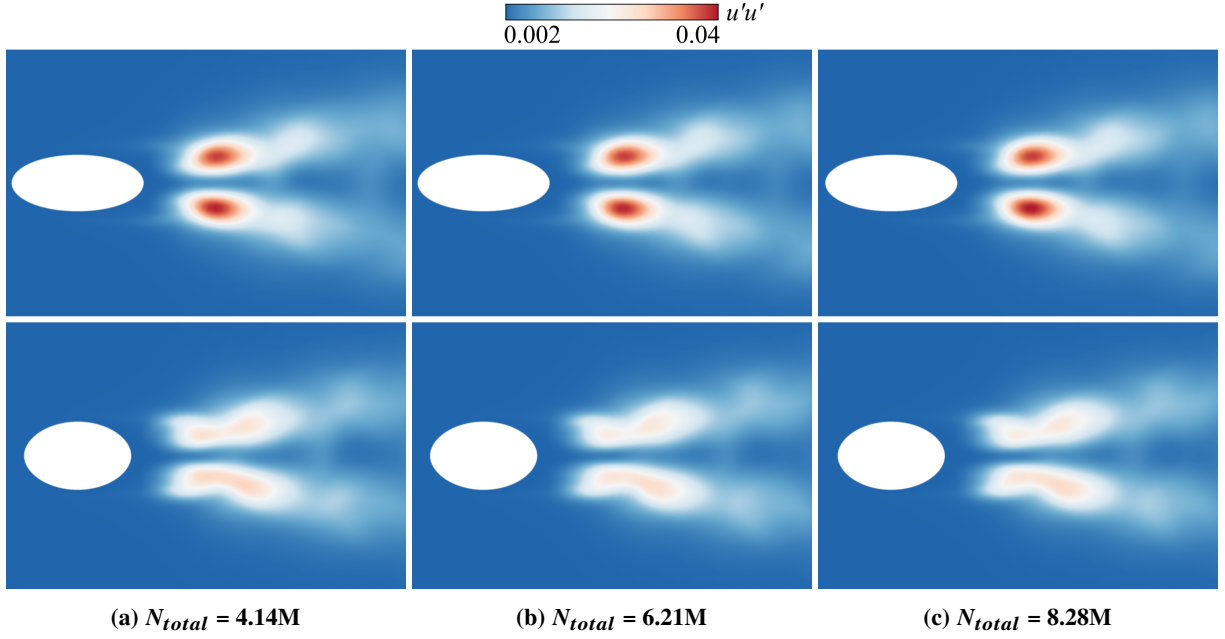


**Fig. A1** Comparison of time-averaged Reynolds stress  $\overline{u'u'}$  on equal colorbars for candidate meshes at locations of  $z/\lambda = 1$  (top) and  $z/\lambda = 0.5$  (bottom) along the span.

**Table A1** Mesh parameters for each tested grid with resulting force and shedding frequency values. The dimensions listed are total nodes  $N_{total}$ , nodes in the spanwise direction  $N_z$ , azimuthal direction  $N_\theta$ , radial direction  $N_r$ , and the resulting cell sizes in the spanwise direction  $\Delta z/T$ , and minimum in the radial direction  $\Delta r/T_{min}$ .

$N_{total}$	$N_z$	$N_\theta$	$N_r$	$\Delta z/T$	$\Delta r/T_{min}$	$\overline{C_D}$	$St$
4.14M	170	160	154	0.041	0.003	0.236	0.1067
6.21M	255	160	154	0.027	0.003	0.234	0.1067
8.28M	340	160	154	0.020	0.003	0.234	0.1067

## References

- [1] Dehnhardt, G., Mauck, B., and Bleckmann, H., “Seal whiskers detect water movements,” *Nature*, Vol. 394, No. 6690, 1998, pp. 235–236. <https://doi.org/10.1038/28303>, URL <https://www.nature.com/articles/28303>.
- [2] Dehnhardt, G., Mauck, B., Hanke, W., and Bleckmann, H., “Hydrodynamic Trail-Following in Harbor Seals (*Phoca vitulina*),” *Science*, Vol. 293, No. 5527, 2001, pp. 102–104. <https://doi.org/10.1126/science.1060514>, URL <http://science.sciencemag.org/content/293/5527/102>.
- [3] Murphy, C. T., Reichmuth, C., Eberhardt, W. C., Calhoun, B. H., and Mann, D. A., “Seal Whiskers Vibrate Over Broad Frequencies During Hydrodynamic Tracking,” *Scientific Reports*, Vol. 7, No. 1, 2017. <https://doi.org/10.1038/s41598-017-07676-w>, URL <https://doi.org/10.1038/s41598-017-07676-w>.
- [4] Hanke, W., Witte, M., Miersch, L., Brede, M., Oeffner, J., Michael, M., Hanke, F., Leder, A., and Dehnhardt, G., “Harbor seal vibrissa morphology suppresses vortex-induced vibrations,” *Journal of Experimental Biology*, Vol. 213, No. 15, 2010, pp. 2665–2672. <https://doi.org/10.1242/jeb.043216>, URL <http://jeb.biologists.org/content/213/15/2665>.
- [5] Lyons, K., Murphy, C. T., and Franck, J. A., “Flow over seal whiskers: Importance of geometric features for force and frequency response,” *PLOS ONE*, Vol. 15, No. 10, 2020, p. e0241142. <https://doi.org/10.1371/journal.pone.0241142>, URL <https://journals.plos.org/plosone/article?id=10.1371/journal.pone.0241142>.
- [6] Rinehart, A., Shyam, V., and Zhang, W., “Characterization of seal whisker morphology: implications for whisker-inspired flow control applications,” *Bioinspiration & Biomimetics*, Vol. 12, No. 6, 2017. <https://doi.org/10.1088/1748-3190/aa8885>, URL <http://stacks.iop.org/1748-3190/12/i=6/a=066005>.
- [7] Zheng, X., Kamat, A., Cao, M., and Kottapalli, A. G. P., “Creating underwater vision through wavy whiskers: a review of the flow-sensing mechanisms and biomimetic potential of seal whiskers,” *J. R. Soc. Interface*, Vol. 18, 2021. URL <https://doi.org/10.1098/rsif.2021.0629>.
- [8] Morrison, H. E., Brede, M., Dehnhardt, G., and Leder, A., “Simulating the flow and trail following capabilities of harbour seal vibrissae with the Lattice Boltzmann Method,” *Journal of Computational Science*, Vol. 17, 2016, pp. 394–402. <https://doi.org/10.1016/j.jocs.2016.04.004>, URL <http://linkinghub.elsevier.com/retrieve/pii/S1877750316300424>.
- [9] Lam, K., and Lin, Y. F., “Effects of wavelength and amplitude of a wavy cylinder in cross-flow at low Reynolds numbers,” *Journal of Fluid Mechanics*, Vol. 620, 2009, pp. 195–220. <https://doi.org/10.1017/S0022112008004217>, URL <https://www.cambridge.org/core/journals/journal-of-fluid-mechanics/article/effects-of-wavelength-and-amplitude-of-a-wavy-cylinder-in-crossflow-at-low-reynolds-numbers/A0EF4CB1305D2557E44D260287A688C9>.
- [10] Kim, H., and Yoon, H. S., “Effect of the orientation of the harbor seal vibrissa based biomimetic cylinder on hydrodynamic forces and vortex induced frequency,” *AIP Advances*, Vol. 7, No. 10, 2017. <https://doi.org/10.1063/1.5008658>, URL <http://aip.scitation.org/doi/10.1063/1.5008658>.



- [11] Liu, G., Xue, Q., and Zheng, X., “Phase-difference on seal whisker surface induces hairpin vortices in the wake to suppress force oscillation,” *Bioinspiration & Biomimetics*, Vol. 14, No. 6, 2019. <https://doi.org/10.1088/1748-3190/ab34fe>, URL <https://doi.org/10.1088/1748-3190/ab34fe>.
- [12] Yoon, H. S., Nam, S. H., and Kim, M. I., “Effect of the geometric features of the harbor seal vibrissa based biomimetic cylinder on the flow over a cylinder,” *Ocean Engineering*, Vol. 218, 2020, p. 108150. <https://doi.org/10.1016/j.oceaneng.2020.108150>, URL <https://www.sciencedirect.com/science/article/pii/S0029801820310866>.
- [13] Yuasa, M., Lyons, K., and Franck, J. A., “Simulations of flow over a bio-inspired undulated cylinder with dynamically morphing topography,” *Journal of Fluids and Structures*, Vol. 211, 2022. <https://doi.org/10.1016/j.jfluidstructs.2022.103567>, URL <https://www.sciencedirect.com/science/article/pii/S0889974622000421>.
- [14] Ahmed, A., and Bays-Muchmore, B., “Transverse flow over a wavy cylinder,” *Physics of Fluids A: Fluid Dynamics*, Vol. 4, No. 9, 1992, pp. 1959–1967. <https://doi.org/10.1063/1.858365>, URL <https://aip.scitation.org/doi/10.1063/1.858365>.
- [15] Lam, K., Wang, F., and So, R., “Three-dimensional nature of vortices in the near wake of a wavy cylinder,” *Journal of Fluids and Structures*, Vol. 19, No. 6, 2004, pp. 815–833. <https://doi.org/10.1016/j.jfluidstructs.2004.04.004>, URL <https://linkinghub.elsevier.com/retrieve/pii/S0889974604000568>.
- [16] Lam, K., Wang, F. H., Li, J. Y., and So, R. M. C., “Experimental investigation of the mean and fluctuating forces of wavy (varicose) cylinders in a cross-flow,” *Journal of Fluids and Structures*, Vol. 19, No. 3, 2004, pp. 321–334. <https://doi.org/10.1016/j.jfluidstructs.2003.12.010>, URL <http://www.sciencedirect.com/science/article/pii/S0889974604000271>.
- [17] Zhang, W., Daichin, and Lee, S. J., “PIV measurements of the near-wake behind a sinusoidal cylinder,” *Experiments in Fluids*, Vol. 38, No. 6, 2005, pp. 824–832. <https://doi.org/10.1007/s00348-005-0981-9>, URL <https://doi.org/10.1007/s00348-005-0981-9>.
- [18] Witte, M., Hanke, W., Wieskotten, S., Miersch, L., Brede, M., Dehnhardt, G., and Leder, A., “On the Wake Flow Dynamics behind Harbor Seal Vibrissae – A Fluid Mechanical Explanation for an Extraordinary Capability,” *Results of the DFG Priority Programme 1207 “Nature-inspired Fluid Mechanics” 2006-2012*, edited by C. Tropea and H. Bleckmann, Springer, Berlin, Heidelberg, 2012, pp. 271–289. [https://doi.org/10.1007/978-3-642-28302-4\\_17](https://doi.org/10.1007/978-3-642-28302-4_17), URL [https://doi.org/10.1007/978-3-642-28302-4\\_17](https://doi.org/10.1007/978-3-642-28302-4_17).
- [19] Shatz, L. F., and Groot, T. D., “The Frequency Response of the Vibrissae of Harp Seal, *Pagophilus Groenlandicus*, to Sound in Air and Water,” *PLOS ONE*, Vol. 8, No. 1, 2013. <https://doi.org/10.1371/journal.pone.0054876>, URL <https://journals.plos.org/plosone/article?id=10.1371/journal.pone.0054876>.
- [20] Murphy, C. T., Eberhardt, W. C., Calhoun, B. H., Mann, K. A., and Mann, D. A., “Effect of Angle on Flow-Induced Vibrations of Pinniped Vibrissae,” *PLOS ONE*, Vol. 8, No. 7, 2013. <https://doi.org/10.1371/journal.pone.0069872>, URL <https://journals.plos.org/plosone/article?id=10.1371/journal.pone.0069872>.

- [21] New, T. H., Shi, S., and Liu, Y., "Cylinder-wall interference effects on finite-length wavy cylinders at subcritical Reynolds number flows," *Experiments in Fluids*, Vol. 54, No. 10, 2013, p. 1601. <https://doi.org/10.1007/s00348-013-1601-8>, URL <http://link.springer.com/10.1007/s00348-013-1601-8>.
- [22] Wang, S., and Liu, Y., "Wake dynamics behind a seal-vibrissa-shaped cylinder: a comparative study by time-resolved particle velocimetry measurements," *Experiments in Fluids*, Vol. 57, No. 3, 2016. <https://doi.org/10.1007/s00348-016-2117-9>, URL <https://doi.org/10.1007/s00348-016-2117-9>.
- [23] Assi, G. R. S., and Bearman, P. W., "Vortex-induced vibration of a wavy elliptic cylinder," *Journal of Fluids and Structures*, Vol. 80, 2018, pp. 1–21. <https://doi.org/10.1016/j.jfluidstructs.2018.02.007>, URL <http://www.sciencedirect.com/science/article/pii/S0889974617306382>.
- [24] Lyons, K., Fercak, O., Murphy, C. T., Kamensky, K. M., Cal, R. B., and Franck, J. A., "Effect of wavelength variation in seal whisker models examined with dye visualization and simulation," *Bioinspiration & Biomimetics*, 2021. Under review for publication in *Bioinspiration & Biomimetics*.
- [25] King, R., "Vortex Excited Oscillations of Yawed Circular Cylinders," *Journal of Fluids Engineering*, Vol. 99, No. 3, 1977, pp. 495–501. <https://doi.org/10.1115/1.3448825>, URL <https://doi.org/10.1115/1.3448825>.
- [26] Ramberg, S. E., "The effects of yaw and finite length upon the vortex wakes of stationary and vibrating circular cylinders," *Journal of Fluid Mechanics*, Vol. 128, 1983, pp. 81–107. <https://doi.org/10.1017/S0022112083000397>, URL <https://www.cambridge.org/core/journals/journal-of-fluid-mechanics/article/effects-of-yaw-and-finite-length-upon-the-vortex-wakes-of-stationary-and-vibrating-circular-cylinders/5FA0BDF52F7865D964DF850A4939722E>.
- [27] Williamson, C. H. K., "Oblique and parallel modes of vortex shedding in the wake of a circular cylinder at low Reynolds numbers," *Journal of Fluid Mechanics*, Vol. 206, 1989, pp. 579–627. <https://doi.org/10.1017/S0022112089002429>, URL <https://www.cambridge.org/core/journals/journal-of-fluid-mechanics/article/oblique-and-parallel-modes-of-vortex-shedding-in-the-wake-of-a-circular-cylinder-at-low-reynolds-numbers/A76E6351C11CA14B35F8161C8AF1D651>.
- [28] Snarski, S. R., "Flow over yawed circular cylinders: Wall pressure spectra and flow regimes," *Physics of Fluids*, Vol. 16, No. 2, 2004, pp. 344–359. <https://doi.org/10.1063/1.1627764>, URL <https://doi.org/10.1063/1.1627764>.
- [29] Thakur, A., Liu, X., and Marshall, J. S., "Wake Flow of Single and Multiple Yawed Cylinders," *Journal of Fluids Engineering*, Vol. 126, No. 5, 2004, pp. 861–870. <https://doi.org/10.1115/1.1792276>, URL <https://doi.org/10.1115/1.1792276>.
- [30] Wang, R., Cheng, S., and Ting, D. S.-K., "Effect of yaw angle on flow structure and cross-flow force around a circular cylinder," *Physics of Fluids*, Vol. 31, No. 1, 2019, p. 014107. <https://doi.org/10.1063/1.5079750>, URL <https://doi.org/10.1063/1.5079750>.
- [31] Lucor, D., and Karniadakis, G. E., "Effects of Oblique Inflow in Vortex-Induced Vibrations," *Flow, Turbulence and Combustion*, Vol. 71, No. 1, 2003, pp. 375–389. <https://doi.org/10.1023/B:APPL.0000014929.90891.4d>, URL <https://doi.org/10.1023/B:APPL.0000014929.90891.4d>.

- [32] Marshall, J. S., “Wake Dynamics of a Yawed Cylinder,” *Journal of Fluids Engineering*, Vol. 125, No. 1, 2003, pp. 97–103. <https://doi.org/10.1115/1.1523069>, URL <https://doi.org/10.1115/1.1523069>.
- [33] Zhao, M., Cheng, L., and Zhou, T., “Direct numerical simulation of three-dimensional flow past a yawed circular cylinder of infinite length,” *Journal of Fluids and Structures*, Vol. 25, No. 5, 2009, pp. 831–847. <https://doi.org/10.1016/j.jfluidstructs.2009.02.004>, URL <https://www.sciencedirect.com/science/article/pii/S0889974609000218>.
- [34] Lyons, K., Cal, R., and Franck, J., “Effects of wavelength on vortex structure and turbulence kinetic energy transfer of flow over undulated cylinders,” *Theoretical and Computational Fluid Dynamics*, Vol. 37, 2023, pp. 485—504. <https://doi.org/https://doi.org/10.1007/s00162-023-00661-2>, URL <https://link.springer.com/article/10.1007/s00162-023-00661-2>.
- [35] Dunt, T. K., Heck, K., Lyons, K., Murphy, C., Cal, R., and Franck, J., “Wavelength-induced shedding frequency modulation of seal whisker inspired cylinders,” *Bioinspiration & Biomimetics*, 2024. <https://doi.org/10.1088/1748-3190/ad2b04>, URL <https://iopscience.iop.org/article/10.1088/1748-3190/ad2b04>.
- [36] Wang, S., and Liu, Y. Z., “Flow structures behind a vibrissa-shaped cylinder at different angles of attack: Complication on vortex-induced vibration,” *International Journal of Heat and Fluid Flow*, Vol. 68, 2017, pp. 31–52. <https://doi.org/10.1016/j.ijheatfluidflow.2017.09.006>, URL <https://linkinghub.elsevier.com/retrieve/pii/S0142727X1730632X>.
- [37] Jones, R., “Effects of sweepback on boundary layer and separation,” *National Advisory Committee for Aeronautics Technical Note*, , No. 884, 1947. URL <https://ntrs.nasa.gov/citations/19930091953>.
- [38] “OpenFOAM, a free, open source software for computational fluid dynamics (CFD), developed primarily by CFD Direct, on behalf of the OpenFOAM Foundation. <http://openfoam.org>,” , 2015.
- [39] Lesage, V., Hammill, M., and Kovacs, K., “Functional classification of harbor seal (*Phoca vitulina*) dives using depth profiles, swimming velocity, and an index of foraging success,” *Canadian Journal of Zoology*, Vol. 77, 1999. <https://doi.org/https://doi.org/10.1139/z98-199>, URL <https://cdnsiencepub.com/doi/10.1139/z98-199>.
- [40] Menon, K., Kumar, S., and Mittal, R., “Contribution of spanwise and cross-span vortices to the lift generation of low-aspect-ratio wings: Insights from force partitioning,” *Phys. Rev. Fluids*, Vol. 7, 2022, p. 114102. <https://doi.org/10.1103/PhysRevFluids.7.114102>, URL <https://link.aps.org/doi/10.1103/PhysRevFluids.7.114102>.